NUKLEONIKA 2026;71(3):53–60
doi: 10.2478/nuka-2026-0007

ORIGINAL PAPER

A fast fully connected neural network-based method for random and scattered coincidence correction in polyhedral brain PET

Yuxuan Zhong, Senhao Wang, Xiulian Chen

Abstract. *Background*. Scattered and random coincidences in brain PET imaging introduce significant noise and degrade resolution. Current correction algorithms for these effects are complex and computationally intensive. Fully connected neural network (FCNN) offers strong feature learning capabilities, versatility, and flexibility. Given that the coincidence data in brain PET imaging has relatively few features, FCNNs are well-suited to rapidly establish the relationship between coincidence data information and coincidence event types. *Methods*. Eleven digital brain models were simulated using the Geant4 application for tomographic emission (GATE) [1]. Features extracted from the resulting data were used as inputs, with coincidence type as the target. FCNN was trained on this dataset. Quantitative evaluation was performed using contrast recovery coefficient (CRC), signal-to-noise ratio (SNR), and contrast-to-noise ratio (CNR) metrics. *Results*. FCNN enables rapid filtering of coincidence data outside the brain region and efficiently corrects both random and scattered coincidences within the brain region. After valid coincidence discrimination, the valid coincidence rate remained at 95.60%, while the scatter fraction decreased from 40.60% to 29.01% and the random fraction dropped from 44.65% to 33.85%. Quantitative evaluation demonstrates that the random and scatter coincidence correction (RSC) method significantly enhances image quality when combined with attenuation-corrected (AC), improving the CRC from 0.946 to 0.969, SNR from 10.24 to 19.13, and CNR from 0.402 to 0.496. Conversely, under non-attenuation--corrected (NAC) conditions, RSC improves CRC (0.945 to 0.971) but reduces SNR (11.53 to 9.73) and CNR (0.569 to 0.521), indicating a trade-off between signal purity and statistical noise. *Conclusion*. FCNN effectively reconstructs the true activity distribution of the radioactive source and enhances image contrast, demonstrating promise for clinical real-time brain PET imaging.

Keywords: Fully connected neural network (FCNN) • Polyhedral brain PET • Random coincidence correction • Scattered coincidence correction • Valid coincidence discrimination

Introduction

Positron emission tomography (PET) is a medical imaging technique that utilizes radiotracers, such as 18-FDG, which undergo positron decay within the human brain. These positrons annihilate with electrons, emitting two γ-photons in opposite directions. Scintillation crystals detect these photons within a specific coincidence time window, and the detection times are recorded to calculate the annihilation point, enabling real-time brain imaging.

However, due to Compton scattering and the finite coincidence time window, three types of coincidence events are generated: true coincidences, scattered coincidences, and random coincidences. True coincidences constitute the core data for brain PET imaging, whereas scattered and random

Y. X. Zhong, S. H. Wang, X. L. Chen✉
Sichuan University, Chengdu, Sichuan, China
E-mail: 243861853@qq.com

Received: 15 March 2026
Accepted: 15 June 2026

coincidences introduce significant noise into the reconstructed images.

For scattered coincidence correction, the most practical method currently is single scatter simulation (SSS), along with Monte Carlo (MC) scatter correction and deep learning-based sinogram scatter correction. The SSS method performs well in estimating single scattering events [2]. It requires an auxiliary step to estimate multiple scattering events, typically achieved by scaling the single scatter distribution estimate using tail-fitting techniques to match the measured data distribution, which includes multiple scattering events. This fitting process usually utilizes regions of the sinogram outside the emission source distribution. Depending on the imaging configuration and activity distribution, this process can be inaccurate, primarily because single and multiple scatter distributions have significantly different shapes, along with noise and other data inconsistencies between internal and external scatter distributions [2, 3]. Recent advancements involve dual scatter simulation (DSS) using only a subset of single scatter pairs, enabling absolute scaling and improved scatter correction results [4]. Regarding MC scatter correction, several studies have proposed MC-based scatter coincidence estimation methods [2, 5–7]. These methods have the potential to provide precise scatter estimates but require substantial computational resources, making them too time-consuming for routine clinical use. Although optimization techniques based on hybrid CPU/GPU architectures have been developed over the past decade to accelerate MC-based scatter estimation [8], the computational burden remains significant. As for deep learning (DL) scatter correction, after the training phase, DL offers the possibility of effectively solving complex and time-consuming tasks. Studies have explored the potential of using DL to directly perform scatter and attenuation correction in image space [9–12]. However, this method requires a large amount of training data and has been proven to fail when presented with images exhibiting variable quality and noise levels not encountered during training.

For random coincidence correction, the mainstream method is the singles counting rate technique. This involves introducing a time delay (longer than the coincidence time window) to measure the count rate of random coincidences without true coincidences, which is then subtracted from the total coincidence count [13, 14]. Alternatively, theoretical formulas are used for estimation and subsequent subtraction. The advantage of this method is that it improves the image signal-to-noise ratio (SNR), reduces quantitative errors, and yields more accurate SUV values [15]. However, the singles rate method is sensitive to dead time and detector efficiency, leading to higher errors. It also increases the count rate of coincidence events.

To address the issue of high computational resource consumption associated with correction methods such as SSS and singles counting rate estimation, this paper proposes a method utilizing a FCNN to rapidly filter coincidence data outside the brain region and perform rapid RSC within the brain slice region. Compared to SSS and delayed coincidence window methods, this approach omits complex correction procedures, thereby saving significant computational resources. The FCNN is a fundamental deep learning network with powerful feature learning capabilities, universality, and flexibility [16–19]. Given that the coincidence data required for brain PET imaging has relatively few features, it is highly suitable for rapidly establishing the relationship between coincidence data information and event types.

This paper first introduces the basic imaging principle of brain PET technology. A polyhedral brain PET detector model was constructed based on GATE. Subsequently, the relationship between coincidence data information and event types was investigated using FCNN. Finally, a method based on FCNN for rapid filtering of coincidence data outside the brain region and RSC within the brain slice region is proposed.

GATE simulation

Simulation model construction

Regarding the detector model, polyhedral brain PET offers higher detection efficiency and geometric adaptability compared to conventional ring-shaped brain PET, resulting in the processing of more data within the same timeframe [20–22]. To investigate fast random and scatter correction for polyhedral brain PET, a polyhedral brain PET detector model based on the great rhombicuboctahedron was constructed using the GATE simulation platform. The scintillation crystals selected were LYSO, with dimensions of 4 mm × 4 mm × 20 mm, separated by a 0.2 mm gap. The selection of 4 mm × 4 mm × 20 mm LYSO crystals with a 0.2 mm gap is based on established designs for high-resolution PET scanners [23]. This configuration offers an optimal balance between spatial resolution, detection efficiency, and depth of interaction (DOI) effects [20].

For the phantom model, to closely mimic the actual human brain structure, this study utilized a 3D brain phantom derived from 11 human brains developed by Aubert-Broche *et al*. [24]. This phantom features strict delineations of brain regions and material assignments, allowing for the classification into 12 distinct tissue regions based on pixel values [24]. The corresponding tissue regions and pixel values are listed in Table 1. Each brain phantom model is divided into 362 slices along the axial direction, with each slice measuring 362 pixels × 434 pixels. The voxel size is 0.5 mm × 0.5 mm × 0.5 mm.

Regarding the source model, to construct a high-fidelity digital source, this study employed an anatomy-constrained physiological modeling approach. Taking into account the spatial continuity of tracer uptake and the complexity of microstructures in real biological tissues, we convolved the high-resolution anatomical phantom with a point spread function (PSF). This process effectively

Table 1. Screening performance of the fully connected neural network for the three types of coincidences

	K1	T	R	S	NECR	RF (%)	SF (%)
Training set							
before primary screening	\	720 456	9 663 407	511 561	47 639.89	93.06	41.52
after primary screening	\	709 268	567 957	484 086	285 617.42	44.47	40.57
after secondary discrimination	–0.6	684 933	349 937	274 977	358 158.79	33.81	28.65
Test set							
before primary screening	\	89 947	1 216 793	64 059	5 902.01	93.12	41.59
after primary screening	\	88 371	71 296	60 410	35 485.01	44.65	40.60
after secondary discrimination	–0.6	84 479	43 237	34 518	43 990.17	33.85	29.01

simulates the biological partial volume effect at tissue interfaces, generating a radiotracer activity distribution map with natural gradient transitions, thereby avoiding non-physiological artifacts inherent in ideal step-function models [25, 26]. A linear mapping relationship between pixel values and activity was established. The radiation source consisted of γ-photons with an energy of 511 keV, emitted in opposite directions.

In terms of simulation parameters, the Monte Carlo simulation was configured to emulate a modern clinical TOF-PET scanner. The detector time resolution was set to 300 ps to represent state-of-the-art systems. An energy resolution of 15% at 511 keV was assumed. Data were acquired within a 400–600 keV energy window to reject scattered events. The system dead time was modeled as 110 ns in non-paralyzable mode, and a 5 ns coincidence time window was applied, consistent with established simulation protocols [27].

Simulation procedure

Based on the phantom and source parameters set in the previous section, eleven simulations were conducted. During these simulations, only the brain phantom and source models were varied, while all other settings remained constant. The centers of the phantom, source, and the polyhedral brain PET detector were all aligned at the coordinate origin. When γ-photons emitted from the source interacted with the scintillators, the simulation recorded eight specific pieces of information for each photon: (event ID, time T, deposited energy E, interaction coordinates (X, Y, Z), Compton scattering ID, Rayleigh scattering ID).

Correction methods and evaluation metrics

Neural network architecture

Based on the simulation results, coincidence recombination was performed on the recorded events using a coincidence time window to obtain the initial coincidence events. These coincidence events were subsequently classified into three categories based on Compton scattering occurrence and other information, and corresponding labels were assigned. For the input layer, assuming a coincidence event includes the following information: response event 1 consists of response time T_1, response energy E_1, response coordinates (X_1, Y_1, Z_1), and response event 2 consists of response time T_2, response energy E_2, response coordinates (X_2, Y_2, Z_2). Thus, the input layer for a single coincidence event is represented as a 1×9 vector (T_1–T_2, E_1, X_1, Y_1, Z_1, E_2, X_2, Y_2, Z_2). The output layer is a 1×1 vector, where a value of 10 indicates a true coincidence, 0 indicates a scattered coincidence, and –10 indicates a random coincidence.

To enhance the quality of coincidence data within the training set, a two-stage true coincidence discrimination process was implemented. The first stage involved eliminating coincidence data where the annihilation point was outside a specified cubic volume, determined by calculating the annihilation point for each event. Specifically, the ten digital brain phantoms used for training, testing, and validation were all located within a cubic space defined by X ranging from –90.5 mm to 90.5 mm, Y ranging from –108.5 mm to 108.5 mm, and Z ranging from –90.5 mm to 90.5 mm.

The FCNN training served as the second stage of true coincidence discrimination. For dataset configuration, coincidence data processed from the first eight digital brain simulations were used as the training set, while data from the ninth and tenth simulations were used as the validation set and test set, respectively.

The FCNN was implemented in MATLAB R2025a. To optimize the model architecture and training parameters – including the number of fully connected layers, neurons per layer, initial learning rate, and L2 regularization coefficient – Bayesian optimization was utilized [28]. During this process, 5-fold cross-validation was embedded within every optimization iteration, providing the evaluation feedback necessary for the algorithm to iteratively update and select the optimal hyperparameters [29].

The Bayesian optimization process ran for 59 iterations, at which point the mean squared error (MSE) had converged. The final architecture of the FCNN consists of an input layer, five hidden layers, and an output layer. The input layer accepts a 1×9 vector, and the output layer produces a 1×1 vector. The number of neurons in the five hidden layers are 511, 217, 126, 18, and 1, respectively. A ReLU activation function is applied between each hidden layer. The optimized initial learning rate is 0.0016658, and the L2 regularization coefficient is 0.000024817.

For the K-fold cross-validation, the final result yielded an MSE of 54.313 ± 0.153.

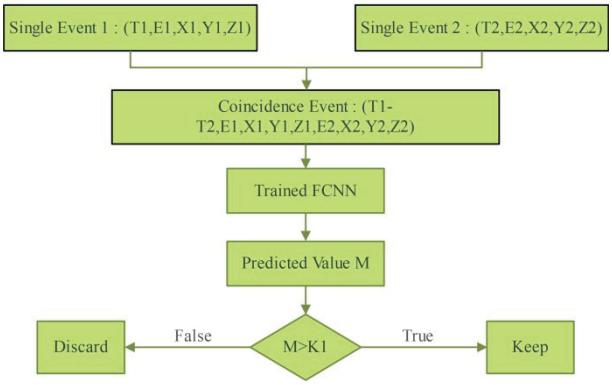

Fig. 1. Schematic illustration of the true coincidence discrimination process.

True coincidence discrimination and random/scatter correction

True coincidence discrimination

As illustrated in Fig. 1, based on the trained network framework, the input layer of the training set is first imported for prediction, yielding a corresponding predicted value M for each coincidence event via FCNN. A lower threshold K is then set to filter coincidence events where M > K, which are presumed to be true coincidences. By comparing these predictions with the actual output layer of the training set and incrementally increasing K, the value K1 is determined when the NECR reaches its maximum. Subsequently, this optimal threshold K1 is applied to the test set to obtain the final predicted NECR.

Random and scatter coincidence correction method

Based on the training results, a correction method for RSC is proposed. The eleventh digital brain phantom is selected to evaluate the training performance. The specific methodology is as follows.

In time-of-flight positron emission tomography (TOF-PET), for a specific line of response (LOR), the system matrix element a_{ij} can be decomposed into the product of a geometric component G_{ij} and a TOF kernel function $K_{ij}(\Delta t)$ [30–32]:

$$a_{ij} = G_{ij} \cdot K_{ij}(\Delta t) \tag{1}$$

Since the types and predicted values M of each coincidence event in the training set are known, the distribution functions of true coincidences, scatter coincidences, and random coincidences with respect to the predicted value M can be denoted as T(M), S(M), and R(M), respectively. The correction function is defined as L(M), expressed by the following equation:

$$L(M) = \frac{T(M)}{T(M) + S(M) + R(M)} \tag{2}$$

For an unknown coincidence event, its predicted value M can be obtained using the trained FCNN. By inputting this M into the correction curve function L(M), the contribution value L of the true coincidence for this event is derived. Based on this true coincidence contribution value L, RSC for the brain PET image can be performed. For a specific LOR, incorporating Eq. (2), it can be expressed as follows:

$$a_{ij} = G_{ij} \cdot K_{ij}(\Delta t) \cdot L \tag{3}$$

To evaluate the training performance, this study employed the single-slice rebinning (SSRB) method to reconstruct images from the coincidence data using the filtered back projection (FBP) algorithm [33, 34]. For 2D voxel assignment along the LOR, a Gaussian kernel function was utilized to distribute values around the annihilation point along the LOR, with a standard deviation of 5 mm. The reconstruction matrix was set to 362 × 434 × 362, with a voxel size of 0.5 mm. The FBP reconstruction matrix image without RSC is denoted as IMG1. The FBP reconstruction matrix image with RSC applied is denoted as IMG2. Furthermore, the FBP reconstruction matrix image generated solely from true coincidence data is denoted as IMG3.

To comprehensively evaluate the performance of the proposed FCNN-based RSC method, both attenuation-corrected (AC) and non-attenuation-corrected (NAC) reconstructions were performed.

For the AC scenario, an analytical attenuation correction was applied. Based on the known anatomical structure and material composition of the digital brain phantom, a theoretical attenuation map (μ-map) was generated. The attenuation factors were then calculated analytically via ray-tracing through this map and applied to the sinogram data prior to reconstruction [35].

It should be noted that the attenuation correction was performed as a standard pre-processing step and was independent of the FCNN model, which focused solely on random and scatter coincidence discrimination.

Evaluation metrics

Evaluation metrics for true coincidence discrimination

To evaluate the performance of true coincidence discrimination, this study adopted the noise equivalent count rate (NECR), scatter fraction (SF), and random fraction (RF). The NECR is primarily used to assess the SNR within the imaging data; a higher NECR indicates lower noise levels in the reconstructed image. The SF measures the proportion of scattered coincidences in the imaging data; a lower SF indicates reduced scatter noise. Similarly, the RF measures the proportion of random coincidences; a lower RF indicates reduced random noise [36, 37].

$$NECR = \frac{T^2}{T + S + R} \tag{4}$$

$$SF = \frac{S}{T + S} \tag{5}$$

$$RF = \frac{R}{T + R} \tag{6}$$

The equation defines T as the number of true coincidences, S as the number of scattered coincidences, and R as the number of random coincidences.

Evaluation metrics for random and scatter coincidence correction

To comprehensively evaluate the performance of random and scatter coincidence correction (RSC) in PET imaging, three key quantitative metrics were employed: the contrast recovery coefficient (CRC), the signal-to-noise ratio (SNR), and the contrast-to--noise ratio (CNR). These metrics collectively assess the accuracy of contrast representation, image clarity, and lesion detectability [38–40].

CRC. The CRC primarily measures the accuracy of contrast recovery in the reconstructed image, reflecting the system's ability to restore the true radioactivity concentration contrast. It is defined as the ratio of the measured contrast in the image to the actual physical contrast. A CRC value closer to 1 indicates superior correction for random and scatter coincidences, implying higher image fidelity and quantitative accuracy.

$$\text{CRC} = \frac{\text{SUV}_{\text{sphere(mean)}}}{\text{SUV}_{\text{background(mean)}}} \Big/ \frac{\text{Activity}_{\text{sphere}}}{\text{Activity}_{\text{background}}} \quad (7)$$

where: $\text{SUV}_{\text{sphere(mean)}}$ – the mean standardized uptake value within the region of interest; $\text{SUV}_{\text{background(mean)}}$ – the mean standardized uptake value within the background region; $\text{Activity}_{\text{sphere}}$ – the true radioactivity concentration in the sphere/lesion region; $\text{Activity}_{\text{background}}$ – the true radioactivity concentration in the background region.

SNR. The SNR reflects the overall clarity of the image by comparing the strength of the desired signal to the level of background noise. A higher SNR indicates a clearer image with less noise interference, which is essential for visual interpretation. In this context, it is calculated based on the maximum signal intensity within the lesion relative to the noise level in a homogeneous reference region.

$$\text{SNR} = \frac{\text{SUV}_{\text{lesion(max)}}}{\sigma_{\text{background}}} \quad (8)$$

where: $\text{SUV}_{\text{lesion(max)}}$ – the maximum standardized uptake value within the lesion/ROI; $\sigma_{\text{background}}$ – the standard deviation of the signal within the background region.

CNR. The CNR evaluates the distinguishability of the target region from the background relative to the noise level. It combines both the contrast difference and the noise characteristics, serving as a critical indicator for assessing lesion detectability. A higher CNR ensures that the contrast between different tissues is significantly greater than the background noise, facilitating accurate diagnosis.

$$\text{CNR} = \frac{\left|\mu_{\text{lesion}} - \mu_{\text{background}}\right|}{\sqrt{\sigma^2_{\text{lesion}} + \sigma^2_{\text{background}}}} \quad (9)$$

where: μ_{lesion} – the mean signal intensity within the lesion; $\mu_{\text{background}}$ – the mean signal intensity within the background region; σ_{lesion} – the standard deviation of the signal within the lesion (representing noise); $\sigma_{\text{background}}$ – the standard deviation of the signal within the background region.

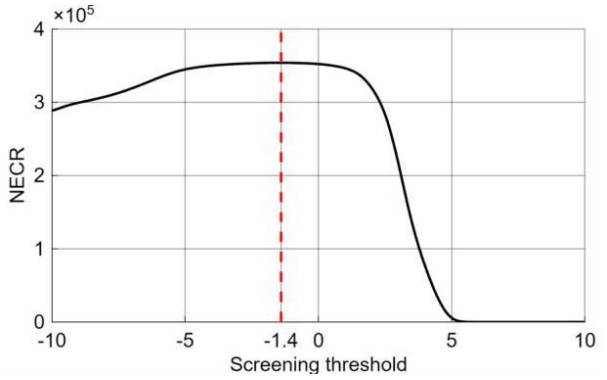

Fig. 2. Variation of the noise equivalent counting rate (NECR) with the lower screening threshold.

Results and analysis

True coincidence discrimination

The GATE simulation required 354 hours, and the deep learning model completed 1 720 000 iterations. The training results demonstrate high computational efficiency: when predicting 1 761 742 coincidence events, the fully connected neural network required only 9.733550 seconds, averaging $5.52495768 \times 10^{-6}$ seconds per event. This indicates the method significantly conserves computational resources and enables rapid prediction for subsequent correction processing.

Figure 2 illustrates the variation of NECR with the lower screening threshold K1. As K1 increases, the NECR gradually rises, reaching a maximum of 353 987.40 when K1 is approximately –0.6. This phenomenon is explained by Fig. 3, which depicts the distribution of predicted values for the three coincidence types and the correction function L(M). The primary reason for setting a lower threshold is that scatter coincidences S(M) and random coincidences R(M) have significant proportions when M< –0.6, whereas L(M) is primarily distributed for M> –0.6. This allows for the easy removal of scatter and random coincidences with predicted values below –0.6. However, in the region where M> –0.6, many random and scatter coincidences remain, as their

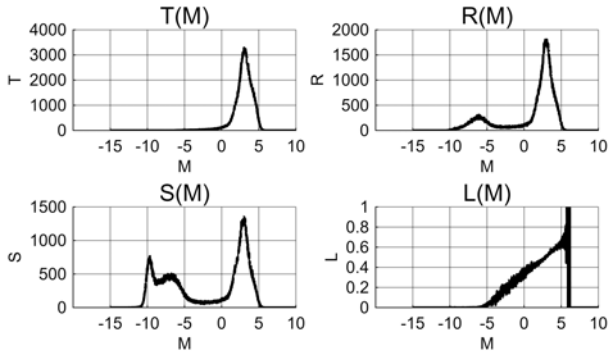

Fig. 3. Schematic diagram of the distribution of predicted values for the three types of coincidences and the correction function.

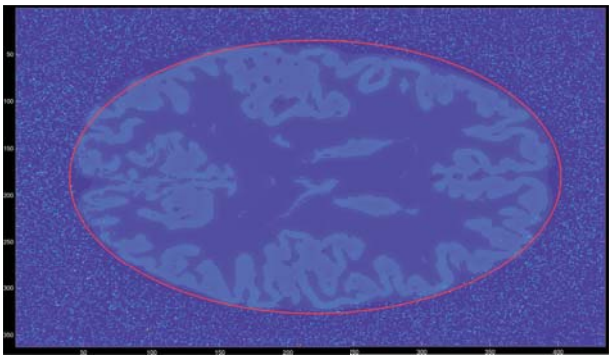

Fig. 4. Example image of the annihilation point probability matrix after screening.

predicted values largely overlap with those of true coincidences, making them difficult to distinguish. Therefore, a secondary discrimination process was implemented.

As shown in Table 1, after secondary discrimination, the NECR of the test set increased from 35 485.01 to 43 990.17. The random fraction (RF) decreased from 44.65% to 33.85%, and the scatter fraction (SF) decreased from 40.60% to 29.01%. Meanwhile, 95.60% of the true coincidences were retained, preserving the core imaging data while significantly reducing random coincidences and thereby minimizing imaging noise interference.

Figure 4 displays the annihilation point probability matrix generated from the filtered coincidence data (predicted values $M < -0.6$) for brain slice 181. The image shows that the filtered annihilation points are predominantly distributed outside the brain slice (outside the red box), with almost no removal of scatter or random coincidences occurring within the brain slice (inside the red box). This demonstrates that the method effectively removes invalid coincidence data outside the brain region, enhancing the quality of the coincidence data for subsequent imaging processing.

Random and scatter coincidence correction

Given the overlap of predicted values for true, random, and scatter coincidences when $M > -0.6$, this paper applied Eq. (3) to perform RSC on this subset of data. As shown in Fig. 5, the CRC, SNR, and CNR were subsequently calculated.

The experimental results demonstrate that the proposed RSC method significantly optimizes image quality when synergistically combined with AC. Under AC conditions, the application of RSC elevated the CRC from 0.946 to 0.969, boosted the SNR substantially from 10.24 to 19.13, and improved the CNR from 0.402 to 0.496 compared to the non-RSC baseline. This confirms the method's effectiveness in purifying the signal through accurate modeling and subtraction of scatter and random events, where AC recovers true count magnitude while RSC removes spurious events, resulting in a synergistic enhancement of contrast recovery and noise suppression.

Conversely, under the NAC condition, the differential impact of RSC on separate metrics necessitates a nuanced explanation grounded in the

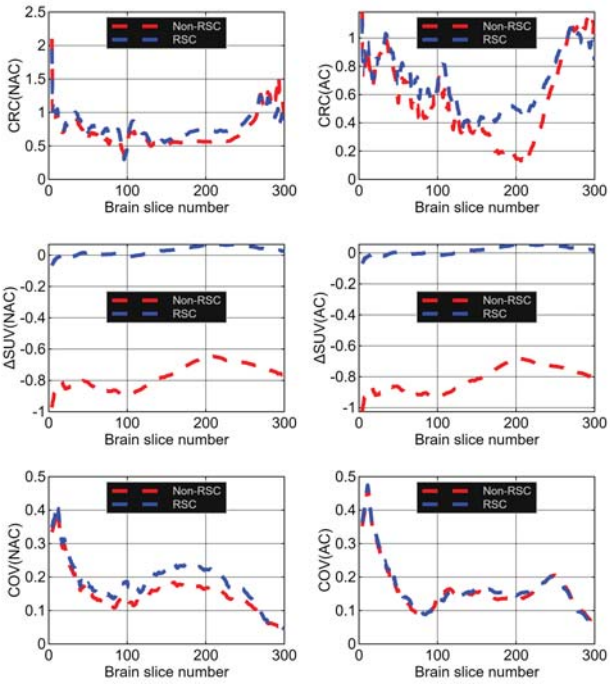

Fig. 5. Comparison of the three metrics before and after attenuation correction.

physical definitions of each parameter. Specifically, the CRC saw a slight increase from 0.945 to 0.971; this marked improvement is a direct consequence of RSC's ability to restore true concentration differences by removing spurious signals that mask true lesions and blur image details, making CRC the most sensitive metric to signal purity. In stark contrast, the SNR deteriorated from 11.53 to 9.73 because the removal of scatter and random components leads to a net loss of total counts without AC compensation, thereby increasing statistical noise according to Poisson statistics (noise $\propto 1/\sqrt{N}$). Consequently, the CNR exhibited an intermediate behavior, decreasing slightly from 0.569 to 0.521, as it represents the composite effect of competing factors where the gain in contrast is offset by the increase in noise.

Therefore, the distinct performance trends observed under NAC do not indicate algorithmic failure but rather reflect the inherent trade-off between physical accuracy and statistical quality, further underscoring that the proposed RSC method is optimally deployed in conjunction with AC.

Conclusion

This study primarily designed a polyhedral brain PET detector based on the great rhombicuboctahedron using Geant4. This detector was employed to simulate the detection of eleven brain phantoms, generating three types of coincidence events. The research focused on methods for the rapid filtering of coincidence data outside the brain region and fast random and scatter coincidence correction within the brain region. By utilizing the inherent time difference, energy, and position information of coincidences as the input layer, a fully connected neural network was trained to establish the mapping

relationship. The output layer's predicted values were then used to discriminate true coincidences and perform random and scatter correction.

The results demonstrate that the fully connected neural network can effectively filter coincidence data outside the brain slices and rapidly perform random and scatter correction within the brain slices. After correction, the metrics showed significant improvement: quantitative evaluation demonstrates that the RSC method significantly enhances image quality when combined with AC, improving the CRC from 0.946 to 0.969, SNR from 10.24 to 19.13, and CNR from 0.402 to 0.496. Conversely, under NAC conditions, RSC improves CRC (0.945 to 0.971) but reduces SNR (11.53 to 9.73) and CNR (0.569 to 0.521), indicating a trade-off between signal purity and statistical noise. The radioactivity concentration in the gray matter regions was accurately recovered, and the method required relatively low computational resources, indicating strong potential for practical application.

Acknowledgments. This work received no specific grant from any funding agency. There are no individuals or institutions to acknowledge.

ORCID

X. L. Chen https://orcid.org/0009-0008-6503-2851
S. H. Wang https://orcid.org/0009-0008-6789-0200
Y. X. Zhong https://orcid.org/0009-0006-8814-2477

References

1. Strulab, D., Santin, G., Lazaro, D., Breton, V., & Morel, C. (2003). GATE (Geant4 application for tomographic emission): a PET/SPECT general-purpose simulation platform. *Nucl. Phys. B-Proc. Suppl.*, *125*, 75–79. DOI: 10.1016/S0920-5632(03)90969-8.
2. Tsoumpas, C., Aguiar, P., Nikita, K. S., Ros, D., & Thielemans, K. (2004). Evaluation of the single scatter simulation algorithm implemented in the STIR library. In IEEE Symposium Conference Record Nuclear Science 2004 (Vol. 6, pp. 3361–3365). IEEE. DOI: 10.1109/nssmic.2004.1466455.
3. Adam, L. E., Karp, J. S., & Brix, G. (1999). Investigation of scattered radiation in 3D whole-body positron emission tomography using Monte Carlo simulations. *Phys. Med. Biol.*, *44*(12), 2879–2895. DOI: 10.1088/0031-9155/44/12/302.
4. Watson, C. C., Newport, D. M. E. C., & Casey, M. E. (1996). A single scatter simulation technique for scatter correction in 3D PET. In P. Grangeat & J. -L. Amans (Eds.), *Three-dimensional image reconstruction in radiology and nuclear medicine* (pp. 255–268). Dordrecht: Springer Netherlands. DOI: 10.1007/978-94-015-8749-5_18.
5. Levin, C. S., Dahlbom, M., & Hoffman, E. J. (1995). A Monte Carlo correction for the effect of Compton scattering in 3-D PET brain imaging. *IEEE Trans. Nucl. Sci.*, *42*(4), 1181–1185. DOI: 10.1109/nssmic.1994.474776.
6. Holdsworth, C. H., Badawi, R. D., Santos, P., Van den Abbeele, A. D., Hoffman, E. J., & El Fakhri, G. (2003). Evaluation of a Monte Carlo scatter correction in clinical 3D PET. In 2023 IEEE Nuclear Science Symposium, 4–11 November 2023, Vancouver, Canada. Conference Record 2023 (IEEE Cat. No. 03CH37515) (Vol. 4, pp. 2540–2544). IEEE. DOI: 10.1109/nssmic.2003.1352408.
7. Bailey, D. L., & Meikle, S. R. (1994). A convolution-subtraction scatter correction method for 3D PET. *Phys. Med. Biol.*, *39*(3), 411–424. DOI: 10.1088/0031-9155/39/3/009.
8. Ma, B., Gaens, M., Caldeira, L., Bert, J., Lohmann, P., Tellmann, L., Lerche, C., Scheins, J., Rota Kops, E., Xu, H., Lenz, M., Pietrzyk, U., & Shah, N. J. (2019). Scatter correction based on GPU-accelerated full Monte Carlo simulation for brain PET/MRI. *IEEE Trans. Med. Imaging*, *39*(1), 140–151. DOI: 10.1109/tmi.2019.2921872.
9. Yang, J., Park, D., Gullberg, G. T., & Seo, Y. (2019). Joint correction of attenuation and scatter in image space using deep convolutional neural networks for dedicated brain 18F-FDG PET. *Phys. Med. Biol.*, *64*(7), 075019. DOI: 10.1088/1361-6560/ab0606.
10. Arabi, H., Bortolin, K., Ginovart, N., Garibotto, V., & Zaidi, H. (2020). Deep learning-guided joint attenuation and scatter correction in multitracer neuroimaging studies. *Human Brain Mapp.*, *41*(13), 3667–3679. DOI: 10.1002/hbm.25039.
11. Shiri, I., Arabi, H., Geramifar, P., Hajianfar, G., Ghafarian, P., Rahmim, A., Reza Ay, M., & Zaidi, H. (2020). Deep-JASC: joint attenuation and scatter correction in whole-body 18F-FDG PET using a deep residual network. *Eur. J. Nucl. Med. Mol. Imaging*, *47*(11), 2533–2548. DOI: 10.1007/s00259-020-04852-5.
12. Liu, F., Jang, H., Kijowski, R., Zhao, G., Bradshaw, T., & McMillan, A. B. (2018). A deep learning approach for 18F-FDG PET attenuation correction. *EJNMMI Phys.*, *5*(1), 24. DOI: 10.1186/s40658-018-0225-8.
13. Brasse, D., Kinahan, P. E., Lartizien, C., Comtat, C., Casey, M., & Michel, C. (2005). Correction methods for random coincidences in fully 3D whole-body PET: impact on data and image quality. *J. Nucl. Med.*, *46*(5), 859–867. DOI: 10.1109/nssmic.2001.1009234.
14. Ollinger, J. M., & Fessler, J. A. (2002). Positron-emission tomography. *IEEE Signal Process. Mag.*, *14*(1), 43–55. DOI: 10.1109/79.560323.
15. Yan, J., Schaefferkoetter, J., Conti, M., & Townsend, D. (2016). A method to assess image quality for low-dose PET: analysis of SNR, CNR, bias and image noise. *Cancer Imaging*, *16*(1), 26. DOI: 10.1186/s40644-016-0086-0.
16. Liang, Y., Xiao, Q., Lu, L., & Xie, J. (2021). FCNN-Lib: A flexible convolution algorithm library for deep learning on FPGAs. *IEEE Trans. Comput.-Aided Des. Integr. Circuits Syst.*, *41*(8), 2546–2559. DOI: 10.1109/tcad.2021.3108065.
17. Aziz, L., Salam, M. S. B. H., Sheikh, U. U., & Ayub, S. (2020). Exploring deep learning-based architecture, strategies, applications and current trends in generic object detection: A comprehensive review. *IEEE Access*, *8*, 170461–170495. DOI: 10.1109/access.2020.3021508.

18. Shawahna, A., Sait, S. M., & El-Maleh, A. (2018). FPGA-based accelerators of deep learning networks for learning and classification: A review. *IEEE Access*, *7*, 7823–7859. DOI: 10.1109/access.2018.2890150.
19. Ahmed, S. F., Alam, M. S. B., Hassan, M., Rozbu, M. R., Ishtiak, T., Rafa, N., Mafijur, M., Shawkat, A. B. M., & Gandomi, A. H. (2023). Deep learning modelling techniques: current progress, applications, advantages, and challenges. *Artif. Intell. Rev.*, *56*(11), 13521–13617. DOI: 10.1007/s10462-023-10466-8.
20. Shi, H., Du, D., Xu, J., Su, Z., & Peng, Q. (2015). Design study of dedicated brain PET with polyhedron geometry. *Technol. Health Care*, *23*(Suppl. 2), S615–S623. DOI: 10.3233/thc-151000.
21. Chen, G., Weng, F., Hong, X., Tao, W., Zhao, Z., Peng, Q., & Huang, Q. (2018). Developing a 'multiPatchPET'system in GATE for a PET system design with irregular geometries. *Phys. Med. Biol.*, *63*(17), 17NT02. DOI: 10.1088/1361-6560/aad8fd.
22. Scheins, J. J., Herzog, H., & Shah, N. J. (2011). Fully-3D PET image reconstruction using scanner-independent, adaptive projection data and highly rotation-symmetric voxel assemblies. *IEEE Trans. Med. Imaging*, *30*(3), 879–892. DOI: 10.1109/tmi.2011.2109732.
23. Niu, M., Liu, Z., Kuang, Z., Wang, X., Ren, N., Sang, Z., Wu, S., Cong, L., Sun, T., Hu, Z., & Yang, Y. (2022). Ultra-high-resolution depth-encoding small animal PET detectors: using GAGG and LYSO crystal arrays. *Med. Phys.*, *49*(5), 3006–3020. DOI: 10.1002/mp.15606.
24. Aubert-Broche, B., Griffin, M., Pike, G. B., Evans, A. C., & Collins, D. L. (2006). Twenty new digital brain phantoms for creation of validation image data bases. *IEEE Trans. Med. Imaging*, *25*(11), 1410–1416. DOI: 10.1109/tmi.2006.883453.
25. Rousset, O. G., Ma, Y., & Evans, A. C. (1998). Correction for partial volume effects in PET: principle and validation. *J. Nucl. Med.*, *39*(5), 904–911.
26. Zubal, I. G., Harrell, C. R., Smith, E. O., Rattner, Z., Gindi, G., & Hoffer, P. B. (1994). Computerized three-dimensional segmented human anatomy. *Med. Phys.*, *21*(2), 299–302. DOI: 10.1118/1.597290.
27. Cañizares, G., Jiménez-Serrano, S., Lucero, A., Morera-Ballester, C., Muñoz, E., Benlloch, J. M., & González, A. J. (2024). Simulation study of clinical PET scanners with different geometries, including TOF and DOI capabilities. *IEEE Trans. Radiat. Plasma Med. Sci.*, *8*(6), 690–699. DOI: 10.1109/TRPMS.2024.3365911.
28. Xiong, J., Ma, Z., Yang, H., Yang, C., & Chen, J. (2025). Bayesian-optimized fully connected neural network for enhanced prediction accuracy in concrete compressive strength estimation. *Civil Environ. Eng.*, *21*(2), 1292–1303. DOI: 10.2478/cee-2025-0095.
29. Anguita, D., Ghelardoni, L., Ghio, A., Oneto, L., & Ridella, S. (2012). The 'K' in K-fold cross validation. In ESANN 2012 Procedings, European Symposium on Artificial Neural Network, Computational Intelligence and Machine Learning, Bruges, Belgium, 25–27 April 2012 (Vol. 102, pp. 441–446). https://hdl.handle.net/11567/539164.
30. Vandenberghe, S., Mikhaylova, E., D'Hoe, E., Mollet, P., & Karp, J. S. (2016). Recent developments in time-of-flight PET. *EJNMMI Phys.*, *3*(1), 3. DOI: 10.1186/s40658-016-0138-3.
31. Mehranian, A., Kotasidis, F., & Zaidi, H. (2016). Accelerated time-of-flight (TOF) PET image reconstruction using TOF bin subsetization and TOF weighting matrix pre-computation. *Phys. Med. Biol.*, *61*(3), 1309–1331. DOI: 10.1088/0031-9155/61/3/1309.
32. Filipović, M., Comtat, C., & Stute, S. (2019). Time-of-flight (TOF) implementation for PET reconstruction in practice. *Phys. Med. Biol.*, *64*(23), 23NT01. DOI: 10.1088/1361-6560/ab4f0b.
33. Vidal, F. P., Rocchisani, J. M., Jia, X., & Jiang, S. B. (2015). Reconstruction in positron emission tomography. In X. Jia & S. B. Jiang (Eds.), *Graphics processing unit-based high performance computing in radiation therapy* (pp. 185–208). CRC Press.
34. Chetih, N., & Messali, Z. (2015). Tomographic image reconstruction using filtered back projection (FBP) and algebraic reconstruction technique (ART). In 2015 3rd International Conference on Control, Engineering & Information Technology (CEIT), 25–27 May 2015 (pp. 1–6). IEEE. DOI: 10.1109/CEIT.2015.7233031.
35. Polycarpou, I., Tsoumpas, C., King, A. P., & Marsden, P. K. (2015). Quantitative evaluation of PET respiratory motion correction using MR derived simulated data. *IEEE Trans. Nucl. Sci.*, *62*(6), 3110–3116. DOI: 10.1109/TNS.2015.2494593.
36. Doss, K. K. M., Mion, P. E., Kao, Y. C. J., Kuo, T. T., & Chen, J. C. (2022). Performance evaluation of a PET of 7T Bruker Micro-PET/MR based on NEMA NU 4-2008 standards. *Electronics*, *11*(14), 2194. DOI: 10.3390/electronics11142194.
37. Li, D., Li, X., Qin, Y., Cheng, Y., & Wang, H. (2013). Radar coincidence imaging: an instantaneous imaging technique with stochastic signals. *IEEE Trans. Geosci. Remote Sensing*, *52*(4), 2261–2277. DOI: 10.1109/tgrs.2013.2258929.
38. Yan, J., Schaefferkoetter, J., Conti, M., & Townsend, D. (2016). A method to assess image quality for low-dose PET: analysis of SNR, CNR, bias and image noise. *Cancer Imaging*, *16*(1), 26. DOI: 10.1186/s40644-016-0086-0.
39. Roy, S., Whitehead, T. D., Quirk, J. D., Salter, A., Ademuyiwa, F. O., Li, S., An, H., & Shoghi, K. I. (2020). Optimal co-clinical radiomics: Sensitivity of radiomic features to tumour volume, image noise and resolution in co-clinical T1-weighted and T2-weighted magnetic resonance imaging. *EBioMedicine*, *59*. DOI: 10.1016/j.ebiom.2020.102963.
40. Pyatykh, S., Hesser, J., & Zheng, L. (2012). Image noise level estimation by principal component analysis. *IEEE Trans. Image Process.*, *22*(2), 687–699. DOI: 10.1109/tip.2012.2221728.